A PATH PLANNING METHOD FOR CROP PHENOTYPING VEHICLES BASED ON UAV RGB IMAGERY AND AN IMPROVED A* ALGORITHM

/

基于无人机 RGB 图像与改进 A*算法的育种表型采集车路径规划方法

Xinyu XIE [1)], Liqun LU [1, *)], Shanshan FU [1)], Hai gang XU [2)], Jing ZHAO [3], Dian long CAO [3)]

[1)] School of Transportation and Vehicle Engineering, Shandong University of Technology, Zibo Shandong 255000, China

[2)] Shandong Shi feng (Group) Company Ltd., Liao Cheng, 252899, China

[3)] College of Agricultural Engineering and Food Science, Shandong University of Technology, Zibo Shandong 255000, China

Tel: 13793332126; E-mail address: luliqun@sdut.edu.cn

Corresponding author: Liqun Lu

DOI: https://doi.org/10.35633/inmateh-78-94

Keywords: *UAV remote sensing; path planning; crop phenotyping vehicle; digital surface model (DSM); traversability analysis; improved A* algorithm*

ABSTRACT

In crop breeding experiments, numerous breeding plots are established, requiring unmanned vehicles to autonomously navigate to designated locations based on breeding material identifiers, for phenotypic data collection. Currently, the identification of navigation target points largely relies on manual measurement. To address this limitation, this study proposes a path planning method for phenotyping vehicles in breeding fields, integrating RGB imagery acquired by unmanned aerial vehicles (UAVs) with an improved A algorithm. The method begins with UAV image mosaicking and geometric correction. Orthophotos and DSMs are then generated. Regions of interest (ROIs) are then extracted and rectified based on affine transformation principles. The colour space of each ROI is converted from RGB to HSV. Rough locations of breeding plots are identified using an energy function method combined with a Savitzky–Golay filter, and precise plot boundaries are subsequently extracted through further application of the energy function method. This approach achieves an average Intersection over Union (IoU) of 95.17% for individual plots, with maximum and minimum rates of 99.8% and 87.8%, respectively. Navigable areas between breeding plots are derived from the DSM. A theoretical roll angle calculation method is developed by simulating the motion of an unmanned vehicle within the field, allowing traversability weights across these areas to be assessed. The A* algorithm is improved by incorporating jump point search (JPS) and diagonal distance heuristics. The improved algorithm then performs path planning by integrating these traversability weights. Simulation results show that the improved algorithm reduces travel distance by 32.12% and planning time by 72.69% compared with the conventional A* algorithm. Field trials in maize breeding plots further validate that the proposed method, based on DSM and the improved A* algorithm, effectively guides unmanned vehicles to avoid highly uneven terrain and select optimal travel paths.*

摘要

*农作物育种小区数量多，无人车需根据育种材料编号自动导航行驶到某一指定位置进行作物育种表型信息采集，目前导航目标点主要依赖人工测量。因此，本文提出了基于无人机 RGB 图像与改进 A*算法的育种表型采集车路径规划方法。对无人机获取的玉米育种田的 RGB 图像进行拼接和校正，生成正射影像和数字地表模型（Digital Surface Model，DSM）。基于图像的仿射变换原理，截取并校正了玉米育种田图像的感兴趣区域。将感兴趣区域的颜色空间从 RGB 转换为 HSV，基于能量函数法和 Savitzky-Golay 滤波器获取育种田块的粗略位置，并再次利用能量函数法获取精确的田块位置，小区获取的分割精度中平均重叠度为 95.17%，最高为 99.8%，最低为 87.8%；基于 DSM 提取育种小区间的可通行区域，通过模拟无人车在田间行走的过程设计了理论横滚角计算方法，计算了可通行区域的通行权重，引入跳点搜索和对角线距离对 A*算法进行了改进，结合通行权重与改进 A*算法进行了路径规划。路径规划仿真试验结果表明，与传统的 A*算法相比，改进后的 A*算法在三种仿真地图环境中的测试结果表明，行驶距离和行驶时间分别平均缩短了 32.12%和 72.69%；无人车在玉米育种田间的试验结果表明，基于 DSM 和改进 A*算法的路径规划能够让无人车避开大的颠簸区域，选择最优路径行驶。*

Xinyu Xie, M.S. Stud. Eng.; Liqun Lu, Assoc. Prof. Ph.D. Eng.; Shanshan Fu, M.S. Stud. Eng.; Hai gang Xu, Engineer; Jing Zhao, Assoc. Prof. Ph.D. Eng.; Dian long Cao, M.S. Stud. Eng.

INTRODUCTION

Traditional crop phenotyping methods rely predominantly on manual operations, which are constrained by low efficiency and inconsistent data quality (*Song et al., 2025*). Currently, automated crop phenotyping platforms (*Depaepe et al., 2025; Faqeerzada et al., 2025*) can be categorised into stationary and mobile systems. Stationary phenotyping platforms can integrate various sensors for data acquisition and offer the advantage of continuous operation; however, their detectable area is relatively fixed, resulting in limited adaptability. The desktop phenotyping platform Crop 3D, developed by the Institute of Botany, Chinese Academy of Sciences, is designed for crops including maize and rice. This system is equipped with multispectral, thermal imaging, and LiDAR sensors for data collection. Integrated with proprietary software for data analysis, it facilitates the extraction of various plant phenotypic parameters, thereby providing valuable data support for crop breeding and growth studies (*Guo et al., 2018*). Mobile phenotyping platforms offer greater flexibility and versatility. *Lu et al. (2021)* constructed a field phenotyping platform consisting of a locomotion system, a control system, and a phenotypic information acquisition system. The platform is outfitted with multiple sensors, including thermal infrared and hyperspectral cameras, to collect phenotypic data. *Lee et al. (2026)* developed a low-cost mobile phenotyping platform that uses three high-resolution action cameras rotating around a plant to record video and reconstructs precise 3D images of each plant via a Structure-from-Motion workflow, which can obtain independent 3D images without moving the plants and thus provide strong support for breeding and genetic research. Crop planting in breeding plots differs from that in large-scale field production—breeding plots are characterised by small area, high variety density, and closely planted specimens. Consequently, the acquisition of phenotypic data from different varieties requires highly precise positioning of the stopping points, which imposes stringent navigation accuracy demands on crop phenotyping vehicles.

Path planning is central to autonomous navigation, with algorithms such as A* (*Chatzisawas et al., 2024; Ge et al., 2023*) and Dijkstra (*Alshammrei et al., 2022; Zhou et al., 2023; Wang et al., 2022*) being widely employed owing to their respective advantages. However, in complex real-world environments, a single path planning algorithm often shows limitations in efficiency, path smoothness, and obstacle avoidance. Consequently, current research demonstrates a distinct trend of shifting from the refinement of individual algorithms towards the integration of multiple approaches to enhance overall system performance. *Yang et al. (2021)* employed the A* algorithm and incorporated an evaluation function along with a turning point fitting method to smooth the planned path, which effectively mitigated issues of path unreasonableness caused by proximity between path points and obstacles. *Shi et al. (2023)* developed an improved simulated annealing algorithm for dynamic path planning that reduces computational effort via initial path selection and deletion operations, outperforming other algorithms in static and dynamic environments. *Gong et al. (2024)* optimised the Dijkstra algorithm using geometric topology methods, resulting in improved smoothness of the planned path and reduced overall path length. *Jiang et al. (2024)* implemented global path planning utilising an optimised A* algorithm and improved the obstacle avoidance performance of the Artificial Potential Field (APF) method through the integration of gravitational potential field correction with a simulated annealing algorithm. A more prevalent trend is the hybridisation of the strengths of different algorithms. *Hou et al. (2020)* employed the Dijkstra algorithm for global path planning and implemented the Dynamic Window Approach (DWA) for local path planning, thereby enhancing the navigation accuracy of robotic platforms. *Wu et al. (2024)* employed the Particle Swarm Optimisation (PSO) algorithm for global search and the Ant Colony Optimisation (ACO) algorithm for local obstacle avoidance, which demonstrates considerable versatility in practical applications. *Shi et al. (2024)* proposed a multi-robot path planning method based on an improved Simulated Annealing (SA) algorithm, which refines the algorithm's operational procedure to rapidly identify the optimal path. *Ganesan et al. (2024)* developed a hybrid-sampling RRT* algorithm (Hybrid-RRT) that balances uniform and non-uniform sampling, achieving 76.14% faster convergence than RRT and reducing node exploration by 48.53% in 2D environments. *Chai et al. (2025)* constructed a three-dimensional model of hilly and mountainous terrain using UAV-based oblique photography. By integrating road boundary extraction with an improved RRT* algorithm, they produced a three-dimensional path incorporating slope information, thus providing a safe and feasible solution for autonomous path planning of agricultural machinery in mountainous regions. However, existing studies mainly focus on geometric path optimisation and obstacle avoidance, with limited consideration of terrain-induced vehicle attitude variations. Furthermore, UAV-derived DSM data are rarely utilised to quantitatively evaluate terrain traversability in agricultural environments. In addition, the high-precision navigation requirements in crop breeding plots remain insufficiently addressed.

To address these challenges, this study proposes a path planning approach based on DSM and an improved A* algorithm. The method utilises UAV-acquired RGB imagery of maize breeding plots to generate the DSM, from which navigable areas and their associated traversability weights are derived. Path planning is subsequently performed utilising an improved A* algorithm that incorporates traversability weight information, thereby enabling high-precision navigation of the phenotyping vehicle across the maize breeding field.

MATERIALS AND METHODS

Study Area Overview

UAV-based RGB image acquisition was conducted at the Hefeng Seed Industry experimental site in Linzi District, Zibo City, Shandong Province, China (118°12′48″E, 36°57′14″N). The site comprises 54 standardized maize breeding plots, each measuring 10 m × 3 m, covering a total area of 1620 m². Each plot contains a single maize breeding material, with 1.8 m wide navigable pathways maintained between adjacent plots. A top-down view of the study area is shown in Fig. 1.

Fig. 1 – Aerial View of the Study Area

UAV RGB Image Acquisition of Maize Breeding Fields

A DJI Phantom 4 RTK unmanned aerial vehicle (UAV), equipped with a DJI FC6310R camera featuring a CMOS sensor, was used to capture visible-light images in JPEG format. The UAV system recorded high-precision positional and attitude data (POS) during image capture. The flight altitude was set at 30 m, and image acquisition was conducted at approximately 12:00 hours local time. The side and forward overlap rates were set at 70% and 80%, respectively. Aerial image mosaicking was conducted using Pix4Dmapper software, and the resulting orthophoto of the maize breeding area is provided in Fig. 2.

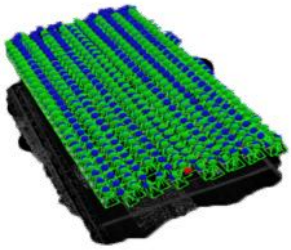

Fig. 2 – Orthophoto of the Maize Breeding Area

Preprocessing of UAV RGB Images of Maize Breeding Plots

In this study, secondary development of the open-source Geospatial Data Abstraction Library (GDAL) was conducted to automate remote sensing data extraction, improving processing efficiency. The Geo TIFF images generated by Pix4D were processed using GDAL. By retrieving the GeoTransform parameters, affine transformations were performed to rotate the imagery, aligning plot boundaries parallel to the coordinate axes and rectifying plot tilt. Subsequently, regions of interest were precisely cropped and geometrically corrected using the transformed coordinates.

The HSV colour space was adopted due to its consistency with human visual perception. Accordingly, visible-light images were converted from RGB to HSV colour space, and plot segmentation was performed using hue and saturation information. Image binarization was conducted based on HSV thresholds for green vegetation (H: 36–77, S: 43–255, V: 46–255) to enhance green plant regions. To reduce the influence of image noise on subsequent processing, Gaussian filtering was applied to the HSV image. Gaussian filtering was applied to suppress noise and smooth the image while preserving edge structures. It effectively suppresses random noise while preserving edge structural information to the greatest extent possible, thus improving the stability and accuracy of subsequent vegetation segmentation and plot boundary extraction.

Experimental Unmanned Ground Vehicle and Navigation System

The experimental unmanned ground vehicle (UGV) used in this study is a tracked mobile platform, with a track width of 140 mm, a track length of 550 mm, and 440 mm between the two tracks. The vehicle is equipped with a single-antenna RTK-GNSS, an electronic compass, and a three-axis gyroscope for positioning, heading control, and roll angle measurement, as shown in Fig. 3. The tracked chassis provides stable support on complex field terrain, and its geometric parameters form the basis for roll angle calculation, traversability assessment, and path planning.

Fig. 3 – Structural Schematic of the Field Phenotyping Vehicle

When the UGV travels along the vertical and horizontal accessible paths within the breeding field, the elevation difference between the ground contact areas of the left and right tracks is used to calculate the theoretical roll angle. This is further utilised to generate traversability weights for optimising the navigation path. To ensure data accuracy, the elevation data within the track contact regions are subjected to statistical filtering of the point cloud to remove outliers, thereby reducing the influence of terrain anomalies and measurement noise on roll angle and weight calculations. By integrating the UGV system with the navigation algorithm, efficient, stable, and autonomous phenotypic data acquisition in breeding fields can be achieved.

Extraction of Breeding Plot Boundaries Based on the Secondary Energy Function Method

During the tasselling stage, gaps between adjacent maize plants cause significant fluctuations in the lateral energy profile. To obtain precise positional information, filtering operations are required for the discrete sequences. Among commonly used filters, the Savitzky–Golay filter effectively suppresses noise while preserving signal shape and the positions of peaks and valleys. A third-order polynomial was used for the least-squares fitting within the sliding window. The sliding window size was empirically determined as 133 pixels according to the inter-plot spacing and image resolution. For breeding plot extraction, local minima in the energy function curve correspond to inter-plot gaps, ensuring accurate boundary localization.

The energy function method is widely used to extract plot boundary regions. Since breeding research focuses on individual plots, identifying the specific plot for each variety is necessary prior to phenotypic data analysis. This method identifies breakpoints between plots by calculating the cumulative energy of green vegetation at specific positions, then connects these breakpoints to form a grid for plot segmentation. The corresponding formula is given in Eq. (1).

$$E(i) = \sum_{j=1}^{N} I(i,j) \tag{1}$$

where:

$I(i,j)$ is the value of the j-th pixel in the i-th row (or column) of the binary image, and N is the total number of pixels in that direction.

In this study, the initial energy function combined with the Savitzky–Golay filter was used to obtain approximate plot locations, followed by subsequent application of the energy function to extract precise boundaries of the maize breeding plots. The resulting segmentation was overlaid on the original RGB image to provide an intuitive visual representation.

To evaluate the accuracy of image segmentation, the Intersection over Union (IoU) metric was utilised to assess the performance of the segmentation results. The IoU is defined in Eq. (2), quantifying the overlap between the regions segmented by the algorithm and the ground truth regions. The ground truth was manually delineated with rectangular bounding boxes in ArcGIS to demarcate the breeding plots. The mean IoU was determined to be 95.17%, with a maximum value of 99.8% and a minimum of 87.8%. The IoU evaluation results are summarised in Table 1.

$$IoU = \frac{TP}{FP + TP + FN} \quad (2)$$

where TP, FP, and FN denote true positive, false positive, and false negative pixels.

Table 1

IoU Calculation Results

Plot ID	IoU (%)	Plot ID	IoU (%)	Plot ID	IoU (%)
F1	98.2	F19	95.6	F37	95.1
F2	97.3	F20	96.8	F38	94.2
F3	95.1	F21	94.4	F39	97.8
F4	98.5	F22	94.8	F40	93.6
F5	92.9	F23	95.9	F41	95.8
F6	95.5	F24	89.4	F42	97.1
F7	93.1	F25	94.1	F43	98.8
F8	96.3	F26	97.8	F44	95.1
F9	98.1	F27	95.2	F45	90.8
F10	99.8	F28	93.6	F46	96.6
F11	97.3	F29	94.3	F47	93.3
F12	96.1	F30	93.5	F48	88.7
F13	95.2	F31	96.4	F49	98.8
F14	96.6	F32	98.8	F50	90.2
F15	98.5	F33	88.1	F51	88.4
F16	96.6	F34	96.8	F52	97.8
F17	97.7	F35	93.6	F53	93.6
F18	98.8	F36	87.8	F54	95.2

Traversability Weight Extraction Algorithm Based on DSM

The precise boundaries of maize breeding plots were obtained using the energy function method. Based on these results, the locations of horizontal and vertical navigable areas between plots, as well as intersection points, were determined. In this study, breeding plots, horizontal navigable areas, vertical navigable areas, and intersection regions were systematically numbered and encoded into a structured graph format. Specifically, 57 horizontal navigable areas (H), 76 intersection regions (C), 72 vertical navigable areas (V), and 54 breeding plots (F) were identified. As shown in Fig. 4, grey cells represent horizontal navigable areas, blue cells indicate intersection regions, white cells denote vertical navigable areas, and green cells correspond to breeding plots.

The Digital Surface Model (DSM) quantifies surface elevation variations, enabling detection of subtle terrain differences challenging to discern with the unaided eye. The DSM is derived from mosaicked imagery through UAV aerial triangulation, representing three-dimensional ground elevation data. It allows rapid analysis of surface height variations. Particularly during the maize tasselling stage, breeding field images closely resemble bare soil; although weeds are present, they remain at the seedling stage and thus have minimal impact on elevation data.

During field-based phenotypic data acquisition, the vehicle's roll angle is the primary factor influencing sensor height variations, directly affecting equipment height stability and phenotypic data quality. The elevation information from DSM can be utilized to assess ground flatness and predict roll angle fluctuations during vehicle traversal.

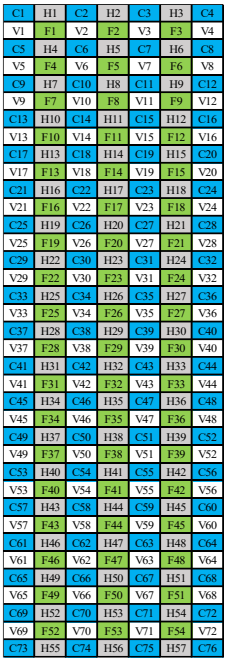

Fig. 4 – Illustration of Traversable Area IDs in the Breeding Plots

The phenotyping vehicle employed in this study adopts a tracked chassis, where the primary factor influencing the vehicle roll angle is the elevation difference of the soil beneath the left and right tracks. By analysing the vertical projection characteristics of the tracks on the DSM image of the breeding plots, the elevation information of the corresponding track regions is extracted, and the theoretical roll angle of the vehicle is calculated. Let z_L and z_R denote the representative elevations of the left and right track regions, respectively, and d represent the distance between the centres of the two tracks. The roll angle can thus be expressed as:

$$R_t = \arctan\left(\frac{z_L - z_R}{d}\right) \tag{3}$$

During computation, the vehicle is assumed to travel along the centreline of the longitudinal accessible region, with a step size of 0.1 m. Statistical filtering is applied to the point cloud data to remove outliers and improve computational accuracy. A statistical outlier removal method was applied: points with elevation values deviating by more than 3σ from the local mean within a radius of 0.1 m were excluded. Accordingly, a sequence of roll angles can be obtained for the vehicle traversing a given region $R_{t1}, R_{t2}, \ldots, R_{tn}$.

The degree of vehicle vibration varies significantly across different regions. To evaluate the traversability of each region, a traversability weight is introduced. A higher weight indicates greater roll angle fluctuation and poorer terrain conditions, whereas a lower weight corresponds to smoother motion and better traversability. To quantitatively characterise the fluctuation of the roll angle, the variance of the roll angle sequence is adopted as the traversability weight, defined as:

$$W_{pass} = \frac{\sum_{i=1}^{n}\left(R_{ti} - \overline{R_t}\right)^2}{n} \tag{4}$$

where $\bar{R_t}$ is the mean value of the roll angle sequence.

Based on the above method, traversability weights are computed for all longitudinal accessible regions (V1–V72) and transverse accessible regions (H1–H57). The results are visualised using a colour gradient, where colours ranging from dark green to red represent increasing traversability weight, as shown in Fig. 5.

Finally, the computed traversability weights are incorporated into the path planning algorithm. By prioritising regions with lower weights, the vehicle preferentially selects paths with smaller roll angle fluctuations, thereby improving motion stability and operational efficiency.

2	2.6	3.14	5.2
1.9	0.9	3.09	1.2
2.4	2	3.86	5.9
1.6	3.9	10.5	4.6
2.9	2.6	17.5	21
1.9	0.8	12.4	2
9.7	3.4	11.7	6.2
7.5	9.6	22	6
12	15	12.8	9.9
7.9	10	11.2	2.7
8.9	2	3.46	6.6
12	1.8	15.3	3.4
14	11	12.8	1.7
31	10	2.71	11
18	7.4	2.05	12
14	8.1	3.06	7.7
17	10	6.77	3.8
11	1.6	3.77	0.9

Distribution of Traversability Weight Parameters for Vertical Areas (V)

7.52	14	53.74
15.9	16.2	28.14
12.3	16.2	18.76
17	19.2	35.47
31.5	19.1	60.95
37.6	15.9	36.13
129	18.2	20.35
57.7	31.5	33.38
45.8	91.1	22.48
14.6	15.9	15.51
26.6	8.36	10.98
21.7	30.5	148.6
23.6	37.9	54.12
60.3	13.8	20.08
29.8	20	44.2
13.5	24.5	72.96
27.3	37.9	664.7
29.7	28.5	53.21

Distribution of Traversability Weight Parameters for Horizontal Areas (H)

Fig. 5 – Spatial distribution of traversability weights

Improvement of the A Algorithm Based on Jump Point Search and Diagonal Distance*

To compare the Dijkstra, Greedy Best-First, and A* algorithms, three environmental configurations were constructed for path planning simulations: (1) a 30 m × 30 m grid map with 25% obstacle ratio; (2) a 40 m × 40 m grid map with 25% obstacle ratio; and (3) a 40 m × 40 m grid map with 40% obstacle ratio. The path planning simulation results of the three algorithms under these three environments are presented in Fig.6.

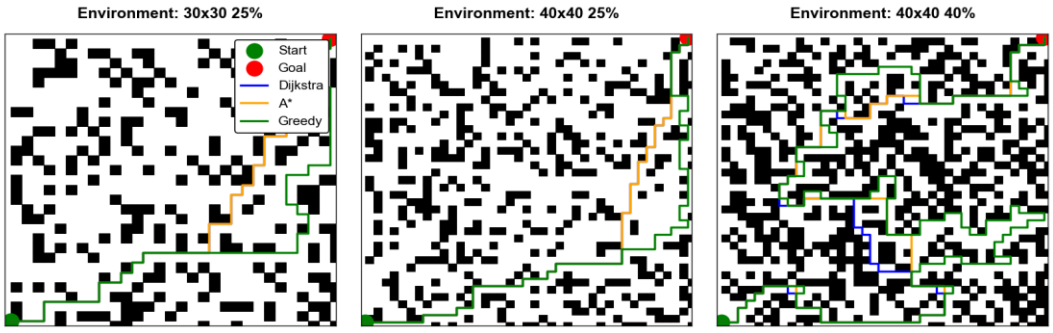

Fig. 6 – Path Planning Simulations of Three Algorithms under Three Different Environments

Based on the simulation results presented above, a comparative analysis of travel path distances and planning durations for the three algorithms was constructed. The path planning outcomes of the three algorithms are provided in Table 2.

Table 2

Path Planning Results of Three Algorithms under Three Different Environments

Environment	Algorithm	Travel Distance (m)	Planning Duration (s)
Environment 1	Dijkstra	58.0	0.0023
	Greedy Best-First	72.8	0.0001
	A*	58.0	0.0006
Environment 2	Dijkstra	78.4	0.0038
	Greedy Best-First	97.2	0.0007
	A*	78.4	0.0025
Environment 3	Dijkstra	98.0	0.0020
	Greedy Best-First	117.2	0.0013
	A*	98.0	0.0008

As indicated in Table 2, the A* algorithm attains shorter travel distances and reduced planning times in comparison with the other algorithms. Therefore, it is selected as the path planning algorithm in this study and further improved.

The improved A* algorithm, shown in Fig. 7, enhances path-planning efficiency and environmental adaptability through the incorporation of a jump-point search strategy and a diagonal distance heuristic.

The improved A* algorithm introduces JPS for node pruning and employs a diagonal distance heuristic to enhance search efficiency. It then proceeds to the iterative expansion phase. In each iteration, if the priority queue is not empty, the node with the smallest estimated total cost $f(n)$ is extracted; if the queue is empty or the target node has been reached, the search is terminated. During neighbourhood expansion of the current node, a jump-point search strategy is applied. In the JPS process, symmetric nodes are pruned based on directional constraints, and only forced neighbours are retained to identify valid jump points. This strategy expands nodes in a leapfrog manner across eight possible directions, directly skipping non-critical nodes that lie along symmetrical or monotonous paths. This method significantly reduces the search space and decreases computational overhead. For feasible nodes, compute their actual cost $g(n)$ and heuristic cost $h(n)$. The diagonal distance is adopted as the heuristic function, and is defined as:

$$h(n) = \max\left(|dx|,|dy|\right) + 0.414 \times \min\left(|dx|,|dy|\right) \quad (5)$$

Additionally, a weighting coefficient $w(p) = 2$ is incorporated into the evaluation function to bias the search toward the target and expedite the search process. The coefficient was empirically set to 2 to balance search speed and path optimality.

The evaluation function is defined as:

$$f(n) = g(n) + w(p) \times h(n) \quad (6)$$

After updating the node's total cost, it is reinserted into the priority queue for subsequent expansion. Concurrently, the node is added to the closed set to avoid redundant exploration. The algorithm iterates through the above steps until either the target node is located, or the priority queue is exhausted. Finally, a pruning optimisation is applied following path generation to remove redundant intermediate nodes, yielding a smoother trajectory with reduced directional changes. This refinement enhances both the practical utility of the route and the motion efficiency of the crop phenotyping vehicle.

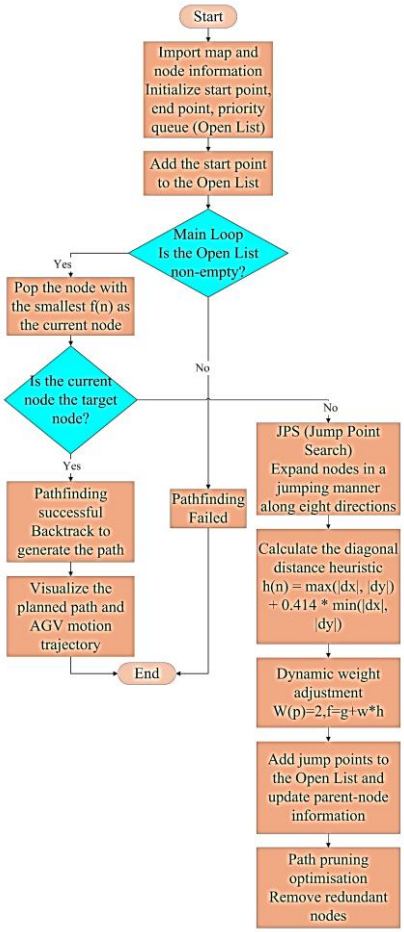

Fig. 7 – Flowchart of the Improved A* Algorithm

Path Planning Based on Traversability Weights and an Improved A* Algorithm

This study utilises high-resolution UAV imagery to construct navigation maps in advance. Compared with waypoint-based pre-marking, this approach offers higher accuracy and more comprehensive environmental information. Compared with real-time mapping, this method involves constructing a pre-established data map, which, when integrated with plot identification, enables improved path planning and contributes to reduced operational costs.

The improved A* algorithm from Section 2.3 is used for path planning in the breeding field. To incorporate terrain information into the path planning process, the cost function of the A* algorithm is modified by introducing traversability weights derived from DSM-based roll angle analysis. The actual cost function is defined as:

$$g(n) = \sum_{i=1}^{k} (d_i + W_i) \tag{7}$$

where:

d_i represents the Euclidean distance between adjacent nodes, and W_i denotes the traversability weight of the corresponding region. Accordingly, the evaluation function is expressed as:

$$f(n) = g(n) + h(n) \tag{8}$$

This formulation enables the algorithm to prioritise regions with lower terrain adaptability while maintaining path optimality.

The traversability weights computed for each horizontal (H) and vertical (V) traversable area serve as the edge costs, accounting for terrain variations. The algorithm then finds the optimal route that minimises the total cost from start to destination.

Vertices represent extracted C regions (intersections of horizontal and vertical traversable areas), and edges represent traversable areas categorized as horizontal (H) and vertical (V), each assigned a cost value. By simplifying the field into a 19×4 Boolean matrix, the graph data structure for breeding plots was initialized, with costs derived from Fig. 8.

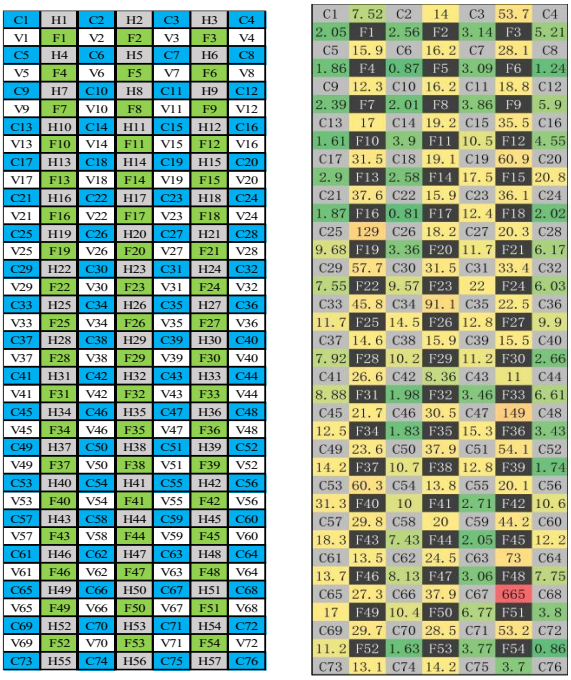

Fig. 8 – Correspondence Table of Codes and Weights

As shown in Fig. 9, when the initial point is defined as C1 and the destination point is set to C76, the optimal path is determined as follows. The waypoints transmitted to the navigation system are (C1→C2→C54→C55→C75→C76). When the initial point is set to C4 and the destination point is set to C73, the optimal path is obtained as follows. The waypoints transmitted to the navigation system are (C4→C56→C55→C75→C73).

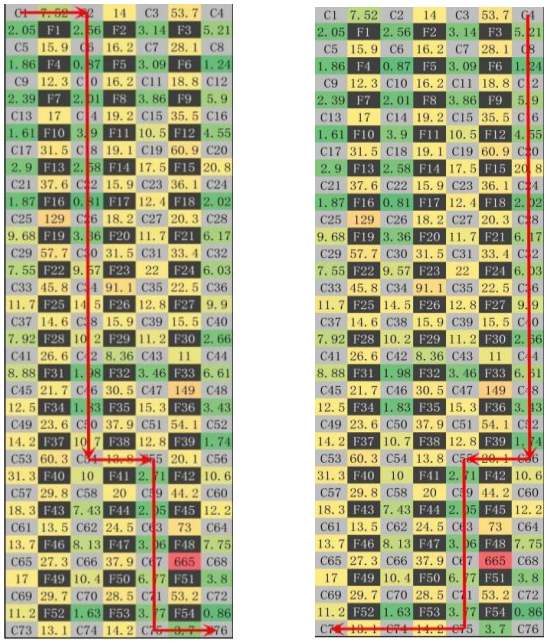

Fig. 9 – Path Planning Results Based on UAV RGB Imagery and the Improved A* Algorithm

RESULTS AND DISCUSSION

Simulation Experiments of the Improved A Algorithm*

To validate the path planning performance of the improved A* algorithm proposed in this paper, comparative simulation experiments were conducted using both the conventional A* algorithm and the improved A* algorithm under three grid map environments of varying scales and obstacle densities. The three environments were configured as follows: Environment 1 was a 30 m × 30 m grid map with a total obstacle ratio of 25%; Environment 2 was a 40 m × 40 m grid map with a total obstacle ratio of 25%; Environment 3 was a 40 m × 40 m grid map with a total obstacle ratio of 40%. These environments respectively simulated a small-scale conventional passage area, a large-scale flat area, and a large-scale densely obstructed area within a breeding field. The simulation results of the A* algorithm and the improved A* algorithm under three different environments are presented in Fig. 10.

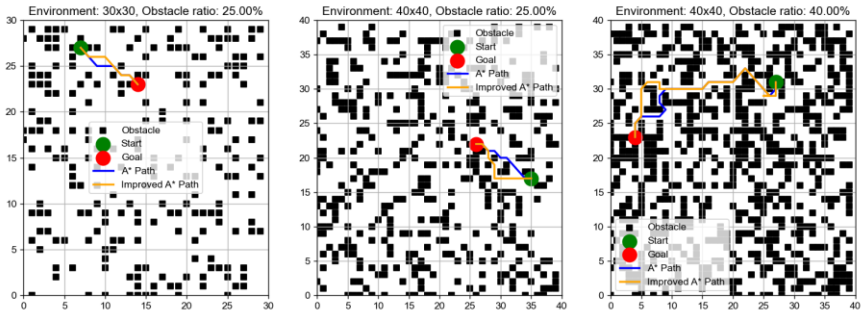

Fig. 10 – Path planning simulations of the A* algorithm and the improved A* algorithm under three different environments

Based on the presented simulation results, a comparative analysis of travel distances and planning durations between the A* algorithm and the improved A* algorithm was constructed. The path planning outcomes are presented in Table 3. As indicated in Table 3, the improved A* algorithm attains shorter travel distances than the standard A* algorithm, demonstrating improved effectiveness. This improvement can be attributed to the pruning mechanism of the jump point search strategy, which reduces redundant node expansions and generates more direct paths.

It should be noted that the travel distances of the standard A* algorithm differ between Table 2 and Table 3 because the simulation configurations were not the same. Table 2 compares three algorithms (Dijkstra, Greedy Best-First, and A*) under three environmental settings with relatively long navigation distances. Table 3, on the other hand, focuses on comparing the conventional A* algorithm with the improved A* algorithm under a different set of simulation scenarios (e.g., map sizes, obstacle distributions, or start-goal pairs). Therefore, the absolute distances reported for A* in the two tables are not directly comparable, and each comparison is valid within its own experimental context.

Table 3

Path Planning Results of the A* Algorithm and the Improved A* Algorithm under Three Different Environments

Environment	Algorithm	Travel Distance (m)	Planning Duration (s)
Environment 1	A*	22.16	0.006
	Improved A*	16.08	0.0002
Environment 2	A*	19.6	0.0033
	Improved A*	10.92	0.0017
Environment 3	A*	34.44	0.0048
	Improved A*	25.96	0.0013

Note: Simulation environments differ between Table 2 and Table 3; therefore, A path lengths are not directly comparable.*

Path Planning Experiments Based on Traversability Weights and Roll Angle

To assess the accuracy of the path planning algorithm, field experiments were carried out at the Eco-UAV Farm of Shandong University of Technology. The weather conditions were clear and calm, the soil was moderately moist, and a significant presence of weeds was observed in the field. The experimental platform consisted of a field phenotyping vehicle.

The study area comprises plots F16, F17, F18, F19, F20, and F21, together with the surrounding traversable regions. The phenotyping vehicle sequentially traverses nine paths, as presented in Fig. 11, from C21 to C32. Each path comprises two vertical and three horizontal traversable segments. By calculating and

summing the traversability costs of the five segments, the actual traversability cost for each path can be determined. The theoretical traversability costs were determined with reference to the cost table presented in Fig. 8.

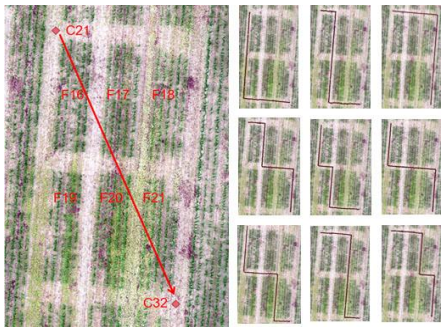

Fig. 11 – Experimental Area for Road Condition Recognition Algorithm Based on DSM

Fig. 12 shows the variation in roll angles measured by the gyroscope and the calculated predicted values in the V21 region adjacent to plot F16. The predicted values generally align with the measured trends. To provide a quantitative indication, we extracted 11 representative points from the curves and estimated the root mean square error (RMSE) to be approximately 1.0° and the mean absolute error (MAE) to be about 0.8°. The mean value of the local minima for both predicted and measured roll angles is approximately 2.7°, indicating that the DSM-derived roll angles effectively simulate the vehicle's roll variations during traversal of the field rows.

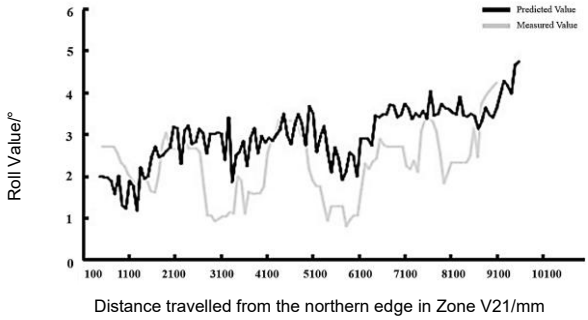

Fig. 12 – Comparison between Predicted Values and Measured Values

Fig. 13 presents the traversability costs from nine path planning experiments. These costs correspond to the traversability weights defined in Section 2.2. Predicted costs were lower than measured values, as the prediction did not account for soil compaction or weed compressibility. Consequently, compressible features such as weeds and soil clumps were treated as obstacles that elevate the vehicle, leading to higher actual costs. Except for the fourth trial, where both predicted and measured costs were relatively low, the results indicate that integrating UAV RGB imagery with the improved A* algorithm enabled the phenotyping vehicle to avoid significant uneven terrain and select optimal routes. Moreover, a consistent trend can be observed between predicted and measured values, demonstrating that the DSM-based traversability weights can effectively reflect terrain-induced variations in vehicle motion.

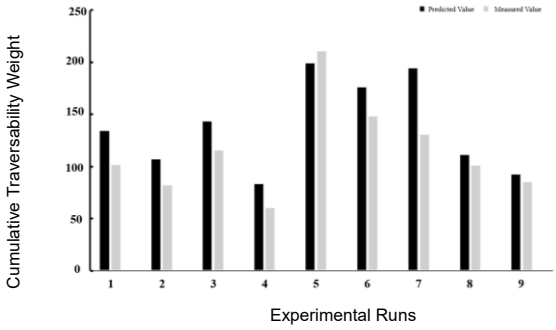

Fig. 13 – Experimental Results of the Optimal Path

Discussion

The proposed method demonstrates clear advantages for integrating terrain information into path planning for crop phenotyping vehicles. Unlike conventional approaches that primarily rely on geometric distance or obstacle distribution, this study incorporates DSM-derived traversability weights based on roll angle estimation, thereby enabling the algorithm to account for terrain-induced vehicle instability.

The improved A* algorithm, combined with jump point search (JPS) and a diagonal distance heuristic, significantly reduces redundant node exploration and enhances computational efficiency. This accounts for the observed reductions in both planning time and travel distance. Compared with existing studies that mainly focus on path smoothness or obstacle avoidance, the proposed approach provides a more comprehensive solution by simultaneously considering terrain adaptability and vehicle stability. This is particularly important in breeding plots characterised by small plot sizes and dense layouts.

Compared with existing studies that mainly focus on geometric optimisation, path smoothness, or obstacle avoidance, the proposed method further incorporates terrain-induced vehicle attitude variations into the path planning process, thereby improving adaptability to complex agricultural environments.

However, several limitations should be acknowledged. The DSM-based model does not account for soil deformation, weed compressibility, or dynamic environmental variations, which may lead to discrepancies between predicted and actual traversability costs. In addition, the method relies on pre-constructed maps and does not yet incorporate real-time perception or dynamic obstacle avoidance. These factors may limit its performance under more complex or rapidly changing field conditions.

Despite these limitations, the experimental results demonstrate that the proposed method achieves a practical balance between computational efficiency and terrain adaptability in structured breeding environments.

CONCLUSIONS

This study proposes a path planning method for crop phenotyping vehicles based on UAV RGB imagery and an improved A* algorithm. By integrating DSM-derived traversability analysis, the method enables vehicles to avoid uneven terrain and achieve stable navigation in breeding fields.

Experimental results demonstrate that the proposed approach improves path planning efficiency while reducing both travel distance and planning time compared with the conventional A* algorithm. The method also demonstrates reliable navigation performance in complex field environments.

Overall, the proposed method provides an effective solution for high-precision navigation in crop breeding plots and offers practical value for intelligent agricultural machinery.

Future work will focus on improving terrain modelling accuracy, incorporating dynamic obstacle avoidance, and extending the method to more diverse agricultural scenarios.

ACKNOWLEDGEMENT

This work was supported by the Central Guidance for Local Science and Technology Development Special Fund (No. YDZX2023086) and the Shandong Provincial Key Research and Development Programme (No. 2024CXPT094).

REFERENCES

[1] Alshammrei S., Boubaker S., Kolsi L., (2022). Improved Dijkstra algorithm for mobile robot path planning and obstacle avoidance, CMC-Computers, *Materials & Continua*, vol.72, no.3, pp.5939-5954, Henderson/USA. DOI: https://doi.org/10.32604/cmc.2022.028165

[2] Chai X., Zhu J., Yao W., Chen C., (2025). A Study on path planning for field roads in hilly and mountainous areas based on low-altitude remote sensing (基于低空遥感的丘陵山地田间道路路径规划研究), *Journal of Hebei Agricultural University*, vol.48, no.1, pp.97-106, Baoding/China. DOI: https://doi.org/10.13320/j.cnki.jauh.2025.0013

[3] Chatzisawas A., Dossis M., Dasygenis M., (2024). Optimizing mobile robot navigation based on A-star algorithm for obstacle avoidance in smart agriculture, *Electronics*, vol.13, no.11, Article 2057, Basel/Switzerland. DOI: https://doi.org/10.3390/electronics13112057

[4] Depaepe T., Ramirez A.I.V., Vandenbussche F., Mishra R., Qureshi R.J., van den Bossche A., van der Straeten D., (2025). MADI: A multispectral automated dynamic imager to monitor plant health, *Plant Phenomics*, vol.7, no.2, pp.100040, Washington/USA. DOI: https://doi.org/10.1016/j.plaphy.2025.100040

[5] Faqeerzada M.A., Park E., Lim J., Kim K., Sathasivam R., Park S.U., Kim H., Cho B.K., (2025). Development of multi-sensing technologies for high-throughput morphological, physiological, and biochemical phenotyping of drought-stressed watermelon plants, *Plant Physiology and Biochemistry*, vol.229, no. Part C, pp.110577, Amsterdam/Netherlands. DOI: https://doi.org/10.1016/j.plaphy.2025.110577

[6] Ganesan S., Ramalingam B., Mohan R.E., (2024). A hybrid sampling-based RRT* path planning algorithm for autonomous mobile robot navigation, *Expert Systems with Applications*, vol.258, pp.125206, Oxford/UK. DOI: https://doi.org/10.1016/j.eswa.2024.125206

[7] Ge H., Ying Z.F., Chen Z.H., Zu W., Liu C.Z., Jin Y.C., (2023). Improved A* algorithm for path planning of spherical robot considering energy consumption, *Sensors*, vol.23, no.16, Article 7115, Basel/Switzerland. DOI: https://doi.org/10.3390/s23167115

[8] Gong H., Ni C., Wang P., Niu Z., Li Y., (2024). A smooth path planning method based on Dijkstra algorithm (基于 Dijkstra 算法的平滑路径规划方法), *Journal of Beijing University of Aeronautics and Astronautics*, vol.50, no.2, pp.535-541, Beijing/China. DOI: https://doi.org/10.13700/j.bh.1001-5965.2022.0377

[9] Guo Q., Yang W., Wu F., Pang S., Jin S., Chen F., Wang X., (2018). High-throughput crop phenotyping: Accelerators for development of breeding and precision agriculture (高通量作物表型监测:育种和精准农业发展的加速器), *Bulletin of Chinese Academy of Sciences*, vol.33, no.9, pp.940-946, Beijing/China. DOI: https://doi.org/10.16418/j.issn.1000-3045.2018.09.007

[10] Hou J., Pu W., Li T., Ding X., (2020). Development of dual-lidar navigation system for greenhouse transportation robot (双激光雷达温室运输机器人导航系统研制), *Transactions of the Chinese Society of Agricultural Engineering*, vol.36, no.14, pp.80-88, Beijing/China. DOI: https://doi.org/10.11975/j.issn.1002-6819.2020.14.010

[11] Jiang X., Wang M., Yang C., Jiang B., (2024). Path planning for orchard spraying robot based on improved A* and APF algorithms (基于 A*和 APF 算法的果园喷雾机器人路径规划), *Transducer and Microsystem Technologies*, vol.43, no.12, pp.145-149, Harbin/China. DOI: https://doi.org/10.13873/J.1000-9787(2024)12-0145-05

[12] Lee S.J., Jo Y.D., (2026). A mobile phenotyping platform for 3D imaging of individual plants using action cameras and structure-from-motion, *Horticulture, Environment, and Biotechnology*, vol.67, pp.197-207, Seoul/South Korea. DOI: https://doi.org/10.1007/s13580-025-00774-z

[13] Lu S., (2021). *Design and experiment of field crop phenotype detection platform (田间作物表型检测平台设计与试验)*, PhD dissertation, Huazhong Agricultural University, Wuhan/China. DOI: https://doi.org/10.27158/d.cnki.ghznu.2021.000362

[14] Shi K., Wu Z.T., Jiang B.P., Karimi H.R., (2023). Dynamic path planning of mobile robot based on improved simulated annealing algorithm, *Journal of the Franklin Institute*, vol.360, no.6, pp.4378-4398, Oxford/UK. DOI: https://doi.org/10.1016/j.jfranklin.2023.01.033

[15] Shi K., Yang L.Y., Wu Z.T., Jiang B.P., Gao Q., (2024). Multi-robot dynamic path planning with priority based on simulated annealing, *Journal of the Franklin Institute*, vol.362, no.1, Article 107396, Oxford/UK. DOI: https://doi.org/10.1016/j.jfranklin.2024.107396

[16] Song P., Li Z., Yang M., Cui J., Feng H., Zhai R., Yang W., (2025). Current status and prospects of crop phenotyping robots (作物表型机器人研究现状与展望), *Transactions of the Chinese Society for Agricultural Machinery*, vol.56, no.3, pp.1-17, Beijing/China. DOI: https://doi.org/10.6041/j.issn.1000-1298.2025.03.001

[17] Wang C., Cheng C., Yang D., Pan G., Zhang F., (2022). Path planning in localization uncertaining environment based on Dijkstra method, *Frontiers in Neurorobotics*, vol.16, Article 821991, Lausanne/Switzerland. DOI: https://doi.org/10.3389/fnbot.2022.821991

[18] Wu Q., Chen H., Liu B., (2024). Path planning of agricultural information collection robot integrating ant colony algorithm and particle swarm algorithm, *IEEE Access*, vol.12, pp.50821-50833, Piscataway/USA. DOI: https://doi.org/10.1109/ACCESS.2024.3385670

[19] Yang Y., Fu K., Jiang T., Liu J., Xiang Z., Cheng Y., (2021). Application of an improved A* algorithm in intelligent vehicle (一种改进 A*算法在智能车中的应用研究), *Journal of Chongqing University of Technology (Natural Science)*, vol.35, no.3, pp.71-79, Chongqing/China. DOI: https://doi.org/10.3969/j.issn.1674-8425(z).2021.03.009

[20] Zhou X., Yan J., Yan M., Mao K., Yang R., Liu W., (2023). Path planning of rail-mounted logistics robots based on the improved Dijkstra algorithm, *Applied Sciences-Basel*, vol.13, no.17, Article 9955, Basel/Switzerland. DOI: https://doi.org/10.3390/app13179955